PUBLICATION 1

Modeling of flow field in polymer electrolyte membrane fuel cell

In: Journal of Power Sources 161(2), pp. 876–884.

Available online at www.sciencedirect.com
ScienceDirect
Journal of Power Sources 161 (2006) 876–884
JOURNAL OF POWER SOURCES
www.elsevier.com/locate/jpowsour

Modeling of flow field in polymer electrolyte membrane fuel cell

Suvi Karvonen [a] *, Tero Hottinen [a], Jaakko Saarinen [b], Olli Himanen [a]

[a] *Helsinki University of Technology, Laboratory of Advanced Energy Systems, P.O. Box 2200, FIN-02015 TKK, Finland*
[b] *VTT Technical Research Centre of Finland, P.O. Box 1601, FI-02044 VTT, Finland*

Received 8 November 2005; received in revised form 7 March 2006; accepted 30 April 2006
Available online 23 June 2006

Abstract

Isothermal two- and three-dimensional polymer electrolyte membrane (PEM) fuel cell cathode flow field models were implemented to study the behavior of reactant and reaction product gas flow in a parallel channel flow field. The focus was on the flow distribution across the channels and the total pressure drop across the flow field. The effect of the density and viscosity variation in the gas resulting from the composition change due to cell reactions was studied and the models were solved with governing equations based on three different approximations. The focus was on showing how a uniform flow profile can be achieved by improving an existing channel design. The modeling results were verified experimentally. A close to uniform flow distribution was achieved in a parallel channel system.

Keywords: PEM fuel cell; PEMFC; Modeling; Flow field plate; Parallel channel; Flow visualization

1. Introduction

Fuel cell is an electrochemical device that converts the chemical energy of reactants into electricity and heat. Fuel cells typically have comparatively high efficiencies and energy densities, in addition to which they have potential as economically friendly power sources. Their properties make them alternative power sources for many applications ranging from portable electronics and vehicles to distributed energy production and power plants. In this study the focus is on the polymer electrolyte membrane fuel cell (PEMFC), but the results can also be applied to other fuel cell types. The PEM fuel cell operates in the temperature range of liquid water, though higher temperature PEM fuel cells are also being developed. PEMFC is in particular suitable for small-scale applications ranging from less than a watt to several kilowatts.

One of the requirements for good cell performance is that the reactants must be distributed as uniformly as possible across the active area of the cell. This is especially important on the cathode side, where the reaction kinetics is comparatively slow and thus forms one of the major performance limiting factors in a PEMFC, the cathode mass transfer overpotential. A non-uniform flow distribution results in a non-uniform reactant distribution, leading to insufficient amounts of reactants on some areas and inhomogeneous current production. In addition to having an adverse effect on cell performance, this can lead to temperature gradients across the active area of the cell, a phenomenon that in an extreme case may damage the membrane. The flow distribution properties also affect the water removal from the cell, and thus a non-uniform flow distribution can cause flooding in the cell.

In a fuel cell stack, the reactant flow is typically directed to each unit cell with a component known as the flow field plate, which also functions as a mechanical support structure and an electrical contact. The flow field plate directs the gas flow into the gas diffusion layer through a channel system, usually molded, etched or machined on the surface of the plate. The flow distribution in the channel system is determined by the relative hydraulic resistances of the channel system. The most common channel configurations are the parallel, serpentine and interdigitated configurations and their combinations, studied in, e.g. [1–9]. The channel system can also be replaced with a porous metal net or foam plate, see, e.g. [10]. The parallel channel configuration, which was studied in this work, typically has a small hydraulic resistance and thus does not generate a large pressure drop across the cell. On the other hand, the parallel channel flow field often has a non-uniform flow distribution and is thus more susceptible to flooding, as many authors have concluded; see, e.g. [5,6,9].

* Corresponding author. Tel.: +358 9 451 3209; fax: +358 9 451 3195.
E-mail address: Suvi.Karvonen@hut.fi (S. Karvonen).

0378-7753/$ – see front matter © 2006 Elsevier B.V. All rights reserved.
doi:10.1016/j.jpowsour.2006.04.145

Nomenclature

A	area (m^2)
D	diffusion coefficient ($m^2\ s^{-1}$)
D_h	hydraulic diameter (m)
e	unit charge (1.6022×10^{-19} C)
F	Faraday's constant ($96485\ C\ mol^{-1}$)
g	gravitational acceleration ($9.8067\ m\ s^{-2}$)
i	current density ($A\ m^{-2}$)
L	characteristic length (m)
M	molar mass ($kg\ mol^{-1}$)
n	surface normal vector
N	number
N_A	Avogadro's constant ($6.022169 \times 10^{23}\ mol^{-1}$)
p	pressure (Pa)
p_0	atmospheric pressure (101.315 kPa)
R	molar gas constant ($8.315\ J\ mol^{---1}\ K^{-1)}$
Re	Reynolds number
s	distance (m)
S_{con}	source term for continuity equation ($kg\ m^{-3}\ s^{-1}$)
$\mathbf{S}_{NS}$	source term for Navier–Stokes equation ($kg\ m^{-2}\ s^{-2}$)
Sh	Sherwood number
t	surface tangential vector
T	temperature (K)
u	total velocity of the fluid ($m\ s^{-1}$)
u	fluid velocity vector ($m\ s^{-1}$)
u_0	inlet velocity ($m\ s^{-1}$)
U	characteristic velocity ($m\ s^{-1}$)
V	volume (m^3)
V_m	molar volume in 343 K ($0.0278\ m^3\ mol^{-1}$)
x	molar fraction
z	number of electrons involved in a reaction

Greek symbols

α	water transport coefficient
Δ	surface roughness (m)
ε	porosity
η	dynamic viscosity (Pas)
λ	stoichiometric constant, 2
ρ	density ($kg\ m^{-3}$)

Subscripts and superscripts

act	active area
air	air
atm	atmospheric
ave	average
Ar	argon
ch	channel
cath	cathode
eff	effective
H_2O	water
in	inlet
lim	limiting
max	maximum
N_2	nitrogen
O_2	oxygen
react	reaction participant
sat	saturated vapor
tot	total
v	vapor

However, these problems can at least partially be avoided with careful design of the flow field system. A uniform flow distribution achieved with the parallel channel system is presented in this work. Consequently, the main result of this work is to show by example that uniform flow distributions can be achieved with parallel channel flow fields with relatively slight changes in the flow field design.

The flow distributions and pressure losses across the channel systems were studied with both two- and three-dimensional one-phase models based on the Navier–Stokes and continuity equations. The changes in the gas density and viscosity along the channels that result from the cell reactions were taken into account in the modeling. The cathode distribution was studied according to three different approximations and the corresponding results were compared in order to find out the error induced by each approximation.

The modeling data and experimental results showed the flow distribution of the original three-dimensional parallel channel system to be polarized. Based on the results, the local hydraulic resistances of the channel system were adjusted through modification of the gas distributor channel. As a result, the modeled polarization was reduced and a close to uniform flow profile was achieved. The modeling results were also experimentally verified and the experimental results were in agreement with the modeling data.

2. Modeling

2.1. Navier–Stokes and continuity equations

The modeling domains consisted of the volume in 3D and cross-sectional area in 2D of the modeled channel systems. Other fuel cell components such as the gas diffusion layer and the membrane electrode assembly were excluded from the model since the focus in this work was on the flow distribution in the flow channels.

The incompressible fluid flow is governed by the time-independent Navier–Stokes and continuity equations:

$$-\rho\mathbf{u}\cdot\nabla\mathbf{u} \quad \rho\mathbf{g} - \nabla p \quad \nabla\cdot(\eta(\nabla\mathbf{u} \quad \nabla\mathbf{u}^{T})) \quad \mathbf{S}_{NS} \tag{1}$$

$$\nabla\cdot(\rho\mathbf{u}) \quad S_{con} \tag{2}$$

which apply to a laminar flow. The flow region, laminar or turbulent, is defined by the Reynolds number, Re:

$$Re \quad \frac{\rho u D_h}{\eta} \tag{3}$$

A flow is laminar when $Re < 2000$. In the studied flow field models the Reynolds number is below 160 and Eqs. (1) and (2) apply to the problem under study.

The source terms in Eqs. (1) and (2), S_{con} and $\mathbf{S}_{NS}$, are calculated from the change in gas composition caused by the cell reactions. The half and full cell reactions of the PEMFC are:

$$\text{anode}: \quad H_2 \rightarrow 2H \quad 2e^- \tag{4}$$

$$\text{cathode}: \quad \tfrac{1}{2}O_2 \quad 2H \quad 2e^- \rightarrow H_2O \tag{5}$$

$$\text{full cell}: \quad \tfrac{1}{2}O_2 \quad H_2 \rightarrow H_2O \tag{6}$$

The continuity equation source term S_{con} is calculated from the mass difference between the consumed oxygen and produced water molecules. The Navier–Stokes source term $\mathbf{S}_{NS}$ is calculated based on the assumption that the kinetic energy and momentum of the oxygen consumed in the reactions are lost into the gas diffusion layer so that the reaction product water has no initial velocity. Thus, the momentum and mass source terms can be written as

$$\mathbf{S}_{NS} \quad -\frac{iA_{act}}{zFV_{ch}} M_{O_2}\mathbf{u} \tag{7}$$

$$S_{con} \quad \frac{iA_{act}}{zFV_{ch}}(\alpha M_{H_2O} - M_{O_2}) \tag{8}$$

where V_{ch} is the volume of the channels crossing the active area of the cell. However, it is likely that some of the kinetic energy and momentum of the consumed oxygen is in fact transferred to the produced water molecules, but estimating the magnitude of this phenomenon is difficult. Therefore, for comparison, the models were also solved using an alternative Navier–Stokes source term calculated by assuming that the kinetic energy and momentum of the consumed oxygen molecules are transferred to the produced water molecules so that their initial velocity equals the average fluid velocity in the channel:

$$\mathbf{S}_{NS\,2} \quad \frac{iA_{act}}{zFV_{ch}}(\alpha M_{H_2O} - M_{O_2})\mathbf{u} \tag{9}$$

The solutions corresponding to the different Navier–Stokes source terms $\mathbf{S}_{NS}$ and $\mathbf{S}_{NS,2}$ gave close to equal results, as the relative differences in the flow velocities were in the order of 10^{-3}. Thus, the possible error made in approximating the Navier–Stokes source term by Eq. (7) should be negligible.

2.2. Approximations

Eq. (1) can be simplified for modeling purposes. According to dimensional analysis the gravity force term $\rho\mathbf{g}$ can be excluded, since its weight is approximately 10^{-3} times the weight of the inertial term:

$$\frac{\rho\mathbf{g}}{\rho\mathbf{u}\cdot\nabla\mathbf{u}} \approx \frac{\rho g}{\rho U^2 \; L} \quad \frac{gL}{U^2} \approx 10^{-3} \tag{10}$$

The channel walls in a flow system can be assumed smooth, if the surface roughness of the wall material is smaller than the limiting surface roughness characteristic to that system [11]:

$$\Delta_{lim} \quad 17\,85\, D_h Re^{-0\,875} \tag{11}$$

With the parameters of the 3D model, $D_h = 0.67$ mm and $Re^{max} = 160$, Eq. (8) gives $\Delta_{lim} = 210$ μm. This is clearly larger than the surface roughness of typical flow field plate materials such as graphite, polymer composite and steel, whose surface roughness is in the order of a few 10 μm or less, see, e.g. [12,13]. However, one of the channel walls is formed by the gas diffusion layer where there is mass transfer through the surface that should be taken into account. Nevertheless, including this effect would complicate the modeling and consequently was excluded here.

The effect of gas cross-over between channels can be neglected since the Sherwood number:

$$Sh \quad \frac{UL}{D^{eff}} \quad \text{where } D^{eff} \quad D\varepsilon^{1\,5} \tag{12}$$

is in the order of 10^3, i.e. the flux in the channels is three orders of magnitude larger than the diffusive flux in the gas diffusion layer. The effect of possible convective flow between the channels is also insignificant since the pressure differences between two parallel channels are very small, at largest a few pascals, which was determined from the solved models.

The current density and temperature in the cell are assumed to be constant across the active area. This is usually not the case in a real fuel cell, where the current density, temperature and flow distribution are all interconnected and also depend on external factors such as the cooling system of the cell. Taking all these issues into account would have made the models very complex and as a consequence required a lot of computing capacity, which was the reason why constant values for these parameters were assumed in this work.

The assumption of one-phase flow, i.e. no liquid water in the channels, is justified if the relative humidity remains lower than 100%. Taking into account the reaction product water of which half is assumed to leave the cell through the cathode side, this applies if the relative humidity of the inlet gases is below 64%, which was calculated assuming a stoichiometry of two and a constant cell temperature of 343 K. These values correspond to the parameter values used in the modeling. In many real fuel cells, the fluid may be in a two-phase flow, and the modeling results gained here do not necessarily apply in these cases. However, high-temperature and low-humidity membranes that function under one-phase flow operating conditions such as assumed in the modeling have been developed (see, e.g. [14–17]) and thus the assumption should be valid for several real fuel cells.

2.3. Model properties

A schematic of the 2D geometry is displayed in Fig. 1. The design of the 3D geometry is similar in principle, but here the distributor channel and the parallel channels crossing the cell are in different planes and the channels are divided into groups of five channels. A schematic of the 3D geometry is presented in Fig. 2. The height of the distributor channel is 1 mm and the height of the parallel channels is 0.5 mm. The cylinders that connect the distributor channel and the parallel channels have a radius of 0.5 mm and height of 2 mm. Each cylinder distributes the flow to five parallel channels and certain periodicity resulting

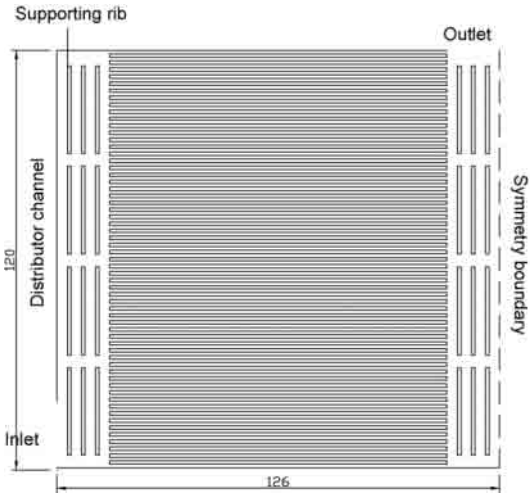

Fig. 1. A schematic of the 2D geometry.

from this can also be seen in the channel flow velocities as will be discussed later in Section 3.2. At the inlet boundaries marked in Figs. 1 and 2, the velocity is fixed: $\mathbf{u}(u\ \ v\ \ w)\quad(u_0\ \ 0\ \ 0)$. At the outlet boundaries also marked in Figs. 1 and 2, the pressure is fixed to zero, $p = 0$. The absolute value of the outlet pressure does not affect the fluid behavior since that is dependent only on the pressure gradients within the flow field, which can be determined from Eq. (1). Due to symmetric channel geometries, only one half of the cathode flow field was modeled. The symmetry boundaries were modeled with the symmetry boundary

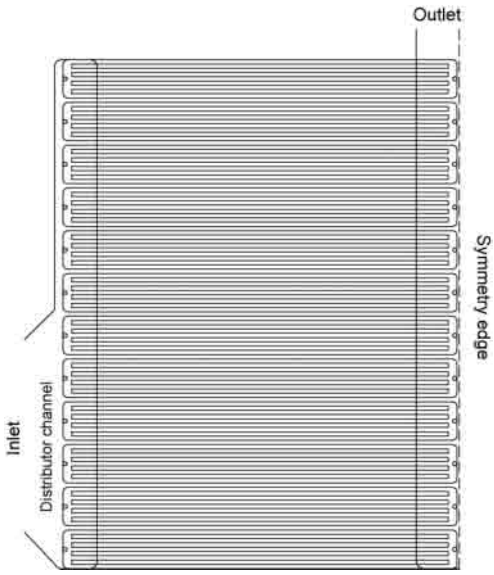

Fig. 2. A schematic of the 3D geometry.

condition:

$$\mathbf{u}\cdot\mathbf{n}\quad 0 \tag{13}$$

$$\mathbf{t}_1\cdot\eta(\nabla\mathbf{u}\quad\nabla\mathbf{u}^{\mathrm{T}})\mathbf{n}\quad 0 \tag{14}$$

and

$$\mathbf{t}_2\cdot\eta(\nabla\mathbf{u}\quad\nabla\mathbf{u}^{\mathrm{T}})\mathbf{n}\quad 0 \tag{15}$$

The majority of the boundaries, corresponding to impermeable channel walls, were governed with the no-slip condition $\mathbf{u} = 0$. It should be noted that the no-slip condition was applied also to the wall formed by the gas diffusion layer in order to avoid further complexity in the modeling, despite the fact that in a real fuel cell mass transfer exists through this boundary.

The inlet flow velocity is calculated from the current density i that was used as a solver parameter:

$$u_0\quad\frac{\dot{n}_{\mathrm{O_2}}}{x_{\mathrm{O_2\ in}}}\frac{RT}{p_0A_{\mathrm{in}}}\quad\frac{RT}{x_{\mathrm{O_2\ in}}p_0}\frac{\lambda A_{\mathrm{act}}}{ez_{\mathrm{cath}}N_{\mathrm{A}}A_{\mathrm{in}}}i \tag{16}$$

where A_{act} is the active area of the cell and A_{in} the cross-sectional area of the inlet. The change in the density and viscosity of the gas in the channels is calculated from the molar fractions of oxygen and water:

$$\begin{aligned}x_{\mathrm{O_2}}(s)\quad&\frac{\dot{n}_{\mathrm{O_2}}}{\dot{n}_{\mathrm{tot}}}\quad\left(\frac{u_{\mathrm{ch}}A_{\mathrm{act}}}{V_{\mathrm{m}}}x_{\mathrm{O_2\ in}}-\frac{iA_{\mathrm{act}}}{z_{\mathrm{cath}}F}\frac{s}{l}\right)\\&\times\left(\frac{u_{\mathrm{ch}}A_{\mathrm{act}}}{V_{\mathrm{m}}}-\frac{iA_{\mathrm{act}}}{z_{\mathrm{cath}}F}\frac{s}{l}\quad 2\alpha\frac{iA_{\mathrm{act}}}{z_{\mathrm{cath}}F}\frac{s}{l}\right)^{-1}\\&\left(x_{\mathrm{O_2\ in}}-\frac{iV_{\mathrm{m}}}{u_{\mathrm{ch}}z_{\mathrm{cath}}F}\frac{s}{l}\right)\\&\times\left(1-(2\alpha-1)\frac{iV_{\mathrm{m}}}{u_{\mathrm{ch}}z_{\mathrm{cath}}F}\frac{s}{l}\right)^{-1}\end{aligned} \tag{17}$$

$$\begin{aligned}x_{\mathrm{H_2O}}(s)\quad&\frac{\dot{n}_{\mathrm{H_2O}}}{\dot{n}_{\mathrm{tot}}}\quad\left(x_{\mathrm{H_2O\ in}}\quad 2\alpha\frac{iV_{\mathrm{m}}}{u_{\mathrm{ch}}z_{\mathrm{cath}}F}\frac{s}{l}\right)\\&\times\left(1-(2\alpha-1)\frac{iV_{\mathrm{m}}}{u_{\mathrm{ch}}z_{\mathrm{cath}}F}\frac{s}{l}\right)^{-1}\end{aligned} \tag{18}$$

The individual channel velocities u_{ch} were calculated by numerical integration across the channel volume separately for each channel:

$$u_{\mathrm{ch}}\quad\frac{1}{V_{\mathrm{ch}}}\sum_{i\ \ 1}^{N}u_iV_i \tag{19}$$

where V_{ch} is the volume (area in 2D) of the channel, N the number of calculation points, u_i and V_i are the velocity at point i and the weight factor at point i (volume in 3D and area in 2D of the space represented by point (i)), respectively. Thus, u_{ch} is the average velocity in the channel.

In the modeling, it was assumed that the water transport coefficient $\alpha = 0.5$, i.e. one half of the product water leaves through the anode side. Thus, the term $2\alpha - 1 = 0$ and the equations for

the molar fractions simplify to:

$$x_{O_2}(s) \quad x_{O_2\ \mathrm{in}} - \frac{iV_m}{u_{ch} z_{cath} F}\frac{s}{l} \tag{20}$$

$$x_{H_2O}(s) \quad x_{H_2O\ \mathrm{in}} \quad 2\alpha\frac{iV_m}{u_{ch} z_{cath} F}\frac{s}{l} \tag{21}$$

These equations were used in the models with the addition that the molar fraction of oxygen cannot be negative and the molar fraction of water has a maximum value corresponding to the situation where all oxygen has been consumed. No acceptable solution can exist outside these limits.

Using the ideal gas law and assuming that dry air is a mixture of oxygen, nitrogen and argon, the density of the gas is calculated from:

$$\rho(s) \quad \frac{(p_{atm} \quad p)(M_{H_2O} x_{H_2O}(s) \quad M_{O_2} x_{O_2}(s) \quad M_{N_2} x_{N_2} \quad M_{Ar} x_{Ar})}{RT} \tag{22}$$

where x_{N_2} and x_{Ar} are constant when $\alpha = 0.5$. The viscosity of the gas mixture is [11]:

$$\eta(s) \quad \left(\frac{x_{H_2O}(s)}{\eta_{H_2O}} \quad \frac{x_{O_2}(s)}{\eta_{O_2}} \quad \frac{x_{N_2}}{\eta_{N_2}} \quad \frac{x_{Ar}}{\eta_{Ar}}\right)^{-1}\frac{\rho(s)}{\rho_{in}} \tag{23}$$

where ρ_{in} is the density of the dry inlet air. The density and viscosity values of the relevant gases as well as their molar fractions in dry standard air are listed in Appendix A.

A non-uniform flow profile makes it easy to study the effect of different approximations on the solution since the differences are usually more prominent at the local minima and maxima. A non-uniform flow profile is easier to accomplish with a 2D geometry due to smaller hydraulic resistance, and thus the modeling was done both in two and three dimensions. In both dimensions, three different modeling schemes were employed to study the effect of the density and viscosity variation:

1. Constant density and viscosity: $\rho = \rho_{air}$ and $\eta = \eta_{air}$. Zero source terms. Continuity equation: $\nabla \cdot \mathbf{u} = 0$.
2. Varying density and viscosity: $\rho = \rho(s)$ and $\eta = \eta(s)$. Zero source terms. Continuity equation: $\nabla \cdot \mathbf{u} = 0$.
3. Varying density and viscosity: $\rho = \rho(s)$ and $\eta = \eta(s)$. Nonzero source terms: S_{con} and $\mathbf{S}_{NS}$. Continuity equation: $\nabla \cdot (\rho \mathbf{u}) = S_{con}$.

The models were solved with the commercially available partial differential equation software FEMLAB®. The calculations were performed over a 64-bit FEMLAB® client-server connection. The server computer was an AMD Athlon64 3500+ with 4GB RAM and 40GB of swap-space. The operating system was SuSe 9.1 AMD64 Linux. The 2D geometry was modeled with 28 000 mesh elements resulting in 160 000 degrees of freedom, whereas the 3D geometry had 180 000 elements and 1.2 million degrees of freedom. In each element, quadratic Lagrange polynomials were used as shape-functions for the components of the velocity field while linear polynomials were used for pressure. The models were solved to as high current densities as the FEMLAB® solver could reach, i.e. 0.35 A cm^{-2} for the 2D geometry and 0.4 A cm^{-2} for the 3D geometry. The experimental parameters corresponded to a 0.5 A cm^{-2} current density, which is the designed operating current for the studied cell and sufficiently close to the 0.4 A cm^{-2} current density of the 3D model for the flow field profiles to be comparable.

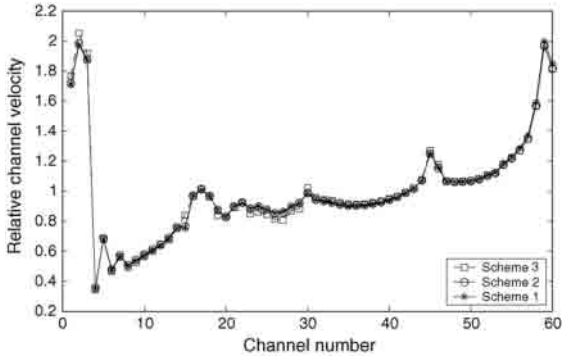

Fig. 3. The relative channel velocities in the 2D model.

3. Results

3.1. 2D geometry

The two-dimensional modeling domain consisted of the cross-sectional area of 60 straight parallel channels and distributor channels as illustrated in Fig. 1. The results discussed here correspond to the highest current density at which the model converged, 0.35 A cm^{-2}. The modeled 2D flow distribution is illustrated in Fig. 3. The channel velocities are taken as the average velocities in the channels integrated over the channel region where the flow is stabilized according to the principle that was presented in Eq. (19). The flow distribution is strongly polarized, as the velocities close to the edges of the flow field plate are more than two times larger than the smallest channel velocities. The lines corresponding to the different approximations are close to indistinguishable. Therefore, the differences in channel velocities predicted by Schemes 1–3 are illustrated in Fig. 4. Based on this data, the maximum differences in relative individ-

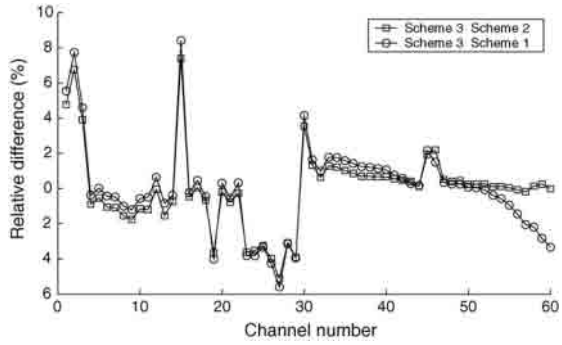

Fig. 4. The relative differences of the results given by the different approximations.

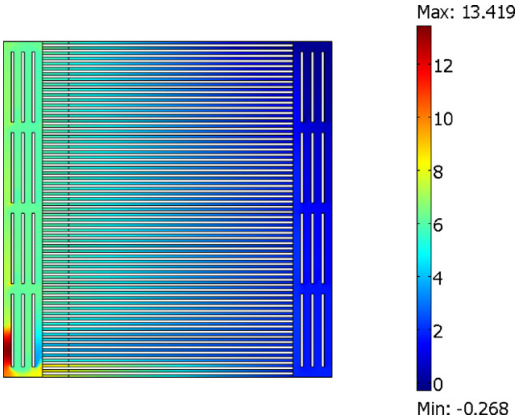

Fig. 5. The pressure distribution in the 2D model. The pressure dimension is pascal (Pa).

ual channel velocities between Schemes 2 and 3 were 7.4% and 8.4% for Schemes 3 and 1. The total pressure losses of Schemes 1 and 2 were 1.1% and 2.3% smaller than that of Scheme 3, respectively. For clarity, the pressure distribution across the 2D geometry corresponding to Scheme 3 with 0.35 A cm^{-2} current density is illustrated in Fig. 5.

3.2. 3D geometry

The three-dimensional model corresponded to an existing parallel channel flow field plate. The modeling results discussed here are the solutions corresponding to the highest current density at which the model converged, which was 0.4 A cm^{-2} for the 3D geometry. The velocity profiles for smaller current densities do not significantly differ from the ones presented here. However, these results do not apply to significantly higher current densities or stoichiometric ratios where the increased flow rate causes more turbulence. The 3D flow-field consisted of 60 channels divided into 12 five-channel groups and distributor channels such as illustrated in Fig. 2.

The relative channel velocities are presented in Fig. 6, where a distinctive five-channel periodicity that derives from the channel system design can be seen in the channel velocities. The flow profile of the 3D model is significantly more uniform than

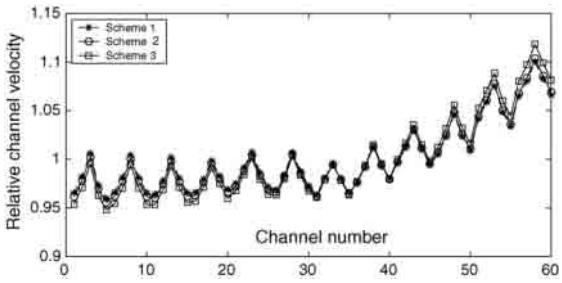

Fig. 6. The relative channel flow velocities of the 3D model.

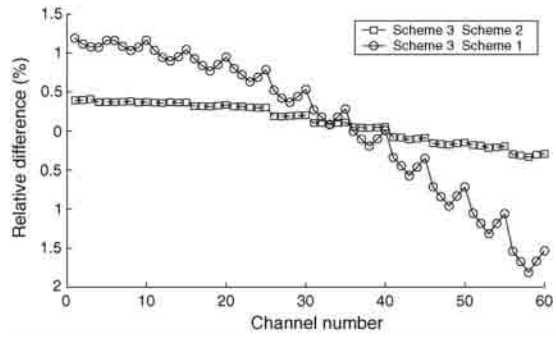

Fig. 7. The relative differences between the different modeling schemes of the original 3D geometry.

that of the 2D model discussed above. The largest individual channel velocity is 16% larger than the smallest. The difference between the largest and smallest five-channel averages is 12%. The differences in relative channel velocities between Schemes 1 and 3 are illustrated in Fig. 7. The maximum differences are 1.8% (Scheme 3 versus Scheme 1) and 0.4% (Scheme 3 versus Scheme 2), significantly smaller than those of the 2D geometry. The channel velocities in Scheme 3 differ more from the velocities in Schemes 1 and 2 in the channels close to the edges of the active area. This follows from the source terms in Scheme 3 that take into account the momentum that is lost into the gas diffusion layer. The total gas flow sees this phenomenon as an increase in the hydraulic resistance on the outlet side. Thus, the channel velocities are slightly larger on the outlet side in Scheme 3. In the 2D model, this effect is more difficult to see since the total differences between Schemes 1 and 3 are significantly larger. The total pressure losses of Schemes 1 and 2 were 9.0% and 7.3% larger than that of Scheme 3, respectively. The pressure distribution across the modified 3D geometry corresponding to Scheme 3 with 0.4 A cm^{-2} current density is illustrated in Fig. 8.

One of the objectives of this work was to achieve a parallel channel flow field, where the flow velocities in different channels

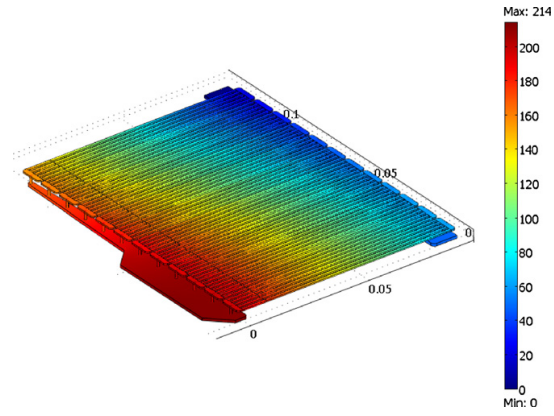

Fig. 8. The pressure distribution in the 3D model. The pressure dimension is pascal (Pa) and the length dimension is meter (m).

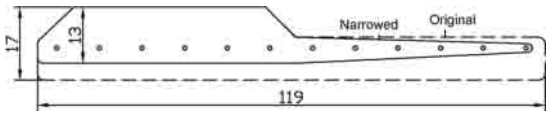

Fig. 9. The original and modified distributor channel geometries.

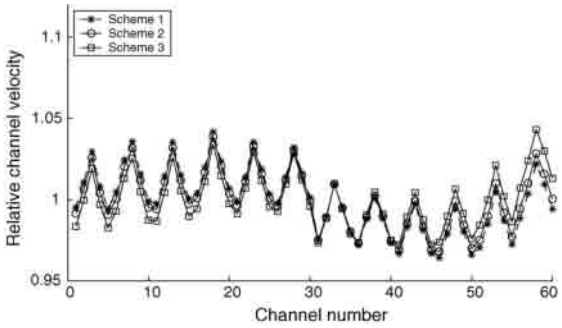

Fig. 10. The close to even channel velocity profile of the modified 3D model.

are close to equal. To accomplish this, the hydraulic resistance of the inlet distributor channel was modified by changing its geometrical shape. The modified distributor channel was optimized for the 0–0.5 A cm^{-2} current density with stoichiometric ratios between 1 and 2. With higher flow rates the velocity distribution will likely become more polarized. Schematics of the original and modified inlet distributor channel geometries are illustrated in Fig. 9.

The velocity profile of this modified 3D geometry is illustrated in Fig. 10. The largest individual channel velocity is approximately 8% larger than the smallest channel velocity, which means that the 16% difference of the original 3D geometry has been reduced to half. When the differences in each five-channel group average are studied, the 12% value of the original 3D geometry has diminished to 3.7%. Thus, the effect of the modification is significant. The differences in relative channel velocities between Schemes 1 and 3 are illustrated in Fig. 11. The maximum differences are 2.1% (Scheme 3 versus Scheme 1) and 0.7% (Scheme 3 versus Scheme 2). These values are

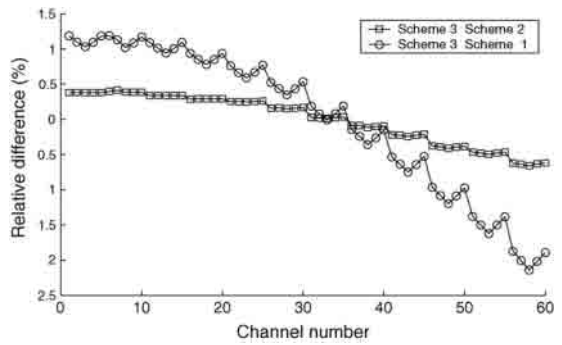

Fig. 11. The relative differences between the different modeling schemes of the modified 3D geometry.

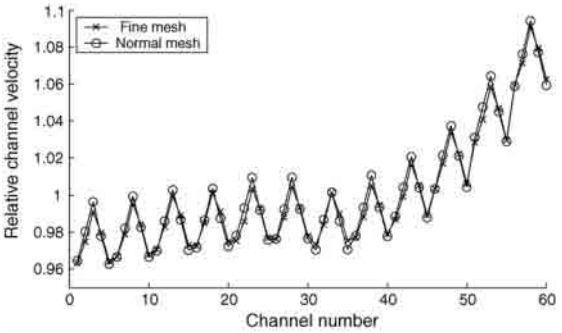

Fig. 12. The relative velocities of the original 3D geometry with two different meshes.

slightly larger than those of the original 3D geometry, which implies that the error made in excluding the source terms or the density and viscosity variation depends on the model geometry to some extent. The total pressure losses of Schemes 1 and 2 were 8.7% and 2.4% larger than that of Scheme 3, respectively.

The effect of the mesh size on the results of the 3D model was studied using a mesh of 220 000 elements for the 3D model and comparing the results to the modeling results presented above with 180 000 elements. The velocity profiles are compared in Fig. 12. The differences are small; the maximum difference in the relative channel velocities is 0.5%. The total pressure differences with the different meshes are within 0.2%. The effect of the mesh was also studied with a single five-channel group, where the number of elements could be grown to four times the original. The relative channel velocities were still within the 0.5% error marginal, but the total pressure difference grew to 5%. This gives reason to expect that the relative channel velocities should be fairly reliable, but that the total pressure difference is more inaccurate. Solving the 3D model with a larger number of elements was not realistic since with the available capacity reaching a solution for the model took from 15 to 40 h with the used mesh.

4. Experimental visualization

The modeling data of the original and modified 3D geometries were verified with experiments. The experimental procedure was simple: dye (water-soluble black ink) was mixed to the fluid flow in pulses, and the progress of the dye pulse was recorded with a digital camera. Since mixing dye into the gas flow would have been complicated, the type of fluid was changed from gaseous (air) to liquid (water). In order to conserve the behavior of the flow, the Reynolds number must remain constant in accordance with dimensional analysis. Following from Eq. (3) the product of density and velocity divided by viscosity must remain constant since the hydraulic diameter is not changed. The values of density and viscosity for air and water are listed in Table 1. A similar visualization study utilizing the laser-induced fluorescence method has previously been carried out by Barreras et al. [9].

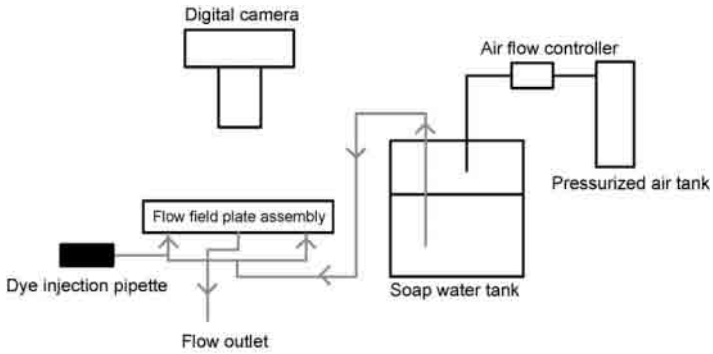

Fig. 13. The experimental arrangement of the flow visualization study. Because of symmetric cell structure, the dye was mixed to only one of the two inlet flows.

The Reynolds number for an air flow in the channels with a flow velocity $u = 1.1\ \mathrm{m\,s^{-1}}$ (corresponding to current density of $i = 0.5\ \mathrm{A\,cm^{-2}}$ at a stoichiometry of two for which the studied cell was designed), is 39. The flow velocity of water in the channels that results in the same Reynolds number is $0.060\ \mathrm{m\,s^{-1}}$, which corresponds to an inlet flow velocity of approximately $200\ \mathrm{ml\,min^{-1}}$.

The flow field plate and endplates were made of transparent polycarbonate. The usual gasket material was replaced with PTFE. The water flow was directed into the flow field plate assembly by pressurizing an air-space in a water tank with a constant $200\ \mathrm{ml\,min^{-1}}$ air flow to provide a stabile flow in the cell assembly. Circulating water through the system caused a part of the channels to be blocked by air bubbles due to the high surface tension of water. Mixing small amounts of soap into the water mostly prevented this phenomenon. The dye was injected with a pipette to the stabilized water flow a few centimeters before the flow entered the cell assembly. The advancing dye pulse was recorded with a Sony® DSC-F828 digital camera. The experimental setup is illustrated in Fig. 13.

The progress of the dye pulse in each five-channel group was studied from the recorded video shots. The flow velocities in each of the 12 five-channel groups were calculated from the time spent by the dye pulse to move through the length of the channels. These calculations were performed with eight sets of experimental data and the results were averaged to give the final values. The error in the channel velocities was taken for both geometries as the maximum average deviation of the individual channel velocities of each measurement set, 4.3% for the original geometry and 5.6% for the modified geometry.

The average velocities of the 12 five-channel groups are compared with the modeled data of the original 3D geometry in Fig. 14. The modeled data, to which the comparisons were made, is that of Scheme 1 (constant density and viscosity), since that is closest to the experimental conditions, where the density and viscosity of the water remain approximately constant. Within the error limits, the experimental results fit the model data, though the experimental velocity profile is more polarized. The stronger polarization is likely due to some systematic error affecting the measurements such as the surface tension of water. Another possibility is that imperfections in the flow field geometry could also have been left in the manufacturing process.

Table 1
Channel velocities corresponding to constant Reynolds number ($Re = 39$) and the densities and viscosities of air and water

	ρ ($\mathrm{kg\,m^{-3}}$)	η (Pas)	Inlet volume flow ($\mathrm{ml\,min^{-1}}$)
Air	1.031401	2.018^{-5}	4104
Water	1000	0.00103	217

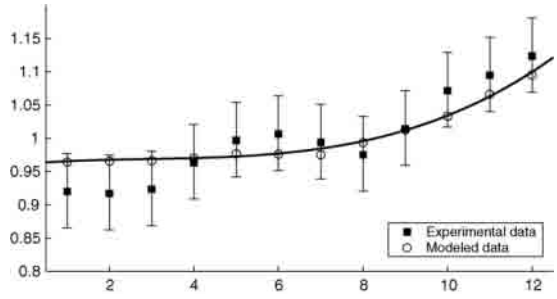

Fig. 14. The experimental and modeling results of the original 3D geometry.

The experiments were also performed with the modified 3D geometry. The results are illustrated in Fig. 15, and the flow profile is more uniform than in Fig. 14 with the original geometry as predicted by the modeling data. Thus, the experiments confirm

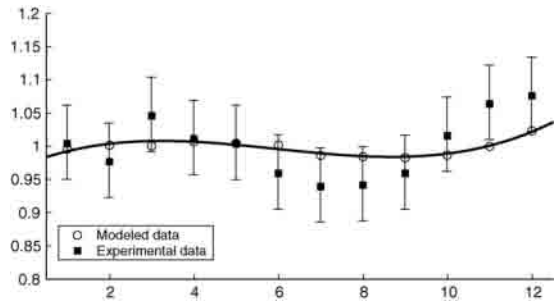

Fig. 15. The experimental and modeling results of the modified 3D geometry.

that the modified geometry should be more advantageous for use in a flow field plate since the reactants should be distributed more uniformly across the active area of the cell.

5. Summary and conclusions

The behavior of fluid flow in an isothermal parallel channel system was modeled with the finite element method. Three modeling schemes based on different approximations were employed in the modeling and the results achieved by these schemes were compared to each other. The modeled 3D parallel channel geometry based on that of a real cell was modified according to modeling data and the improved parallel channel system had nearly uniform flow distribution. The modeled flow profiles were also experimentally verified. The experiments were carried out by recording the progress of a dye pulse in the parallel channels. The distribution of the measured channel velocities was in good correlation with flow distribution predicted by the modeling.

It was discovered that neglecting the density and viscosity variation caused by the cell reactions caused in the case of the 2D geometry at maximum 8% differences in the individual channel velocities. In the case of the close to uniform flow profile of the 3D model this was reduced to 2%. The significance of this error varied between the used geometries, which suggests that in some cases the density and viscosity variation can be neglected, but that this does not hold generally.

However, the results imply that in many cases the effect of excluding the cell reactions on the flow profile is negligible and thus the optimization of the flow field channel system can be done separately from general cell optimization. Uncoupling the flow field channel optimization from the larger cell optimization problem should strongly reduce the required computing capacity. However, the real non-isothermal temperature profile of the cell depends on the cooling system and is likely to have some effect on the flow distribution, offering a subject for further studies.

Based on these conclusions, the 3D parallel channel system was optimized so that a close to uniform flow profile was achieved. Thus, it has been demonstrated in this work that one of the major problems in using the parallel channel system can be overcome with careful design of the flow field plate. This makes the parallel channel flow field a promising alternative due to its typically small pressure losses. The modeling results were verified with experiments and the experimental results were found to be in agreement with the modeling data.

Table A.1
The properties of dry standard air used in the modeling

Component	Molar mass ($g\,mol^{-1}$)	Molar fraction in standard air (%)	η at 343 K (Pas)	ρ at 343 K ($kg\,m^{-3}$)
Nitrogen	28	78	1.97×10^{-5}	0.995
Oxygen	32	21	2.29×10^{-5}	1.137
Argon	40	1	2.60×10^{-5}	1.421
Water	18	0	1.15×10^{-5}	0.64

Acknowledgements

The authors would like to thank the National Technology Agency TEKES and Academy of Finland for funding and VTT Technical Research Centre of Finland for providing flow field plates for the experimental part of the work.

Appendix A

The properties of dry standard air is shown in Table A.1.

References

[1] Z.H. Wang, C.Y. Wang, K.S. Chen, J. Power Sources 94 (2001) 40–50.
[2] L. Wang, H. Liu, J. Power Sources 134 (2004) 185–196.
[3] M. Hu, A. Gu, M. Wang, X. Zhu, L. Yu, Energy Convers. Manage. 45 (2004) 1883–1916.
[4] G. Hu, J. Fan, S. Chen, Y. Liu, K. Cen, J. Power Sources 136 (2004) 1–9.
[5] Y.S. Yoon, W. Lee, S.G. Park, T. Yang, C. Kim, Electrochim. Acta 50 (2004) 705–708.
[6] A. Su, Y.C. Chiu, F.B. Weng, Int. J. Energy Res. 29 (2005) 409–425.
[7] X. Li, I. Sabir, Int. J. Hydr. Energy 30 (2005) 359–371.
[8] G.H. Guvelioglu, H.G. Stenger, J. Power Sources 147 (2005) 95–106.
[9] F. Barreras, A. Lozano, L. Valiño, C. Marín, A. Pascau, J. Power Sources 144 (2005) 54–66.
[10] A. Kumar, R.G. Reddy, J. Power Sources 129 (2004) 62–67.
[11] I.E. Idelchik, Handbook of Hydraulic Resistance, 3rd ed., CRC Press, 1994.
[12] M.H. Oh, Y.S. Yoon, S.G. Park, Electrochim. Acta 50 (2004) 773–776.
[13] S.J. Lee, J.J. Lai, C.H. Huang, J. Power Sources 145 (2005) 362–368.
[14] V. Ramani, H.R. Kunz, J.M. Fenton, J. Membr. Sci. 232 (2004) 31–44.
[15] V. Ramani, H.R. Kunz, J.M. Fenton, Electrochim. Acta 50 (2005) 1181–1187.
[16] S. Yoshioka, A. Yoshimura, H. Fukumoto, O. Hiroi, H. Yoshiyasu, Fuel Cells Bull. 2005 (2005) 11–15.
[17] V. Ramani, H.R. Kunz, J.M. Fenton, J. Power Sources 152 (2005) 182–188.